Journal of Computational Physics 229 (2010) 4075–4096

Contents lists available at ScienceDirect

Journal of Computational Physics

journal homepage: www.elsevier.com/locate/jcp

A hybrid Finite Integration–Finite Volume Scheme

S. Schnepp [a,*,1], E. Gjonaj [b], T. Weiland [b]

[a] Graduate School of Computational Engineering, Technische Universität Darmstadt, Dolivostr. 15, 64293 Darmstadt, Germany
[b] Institut für Theorie Elektromagnetischer Felder, TEMF, Technische Universität Darmstadt, Schloßgartenstr. 8, 64289 Darmstadt, Germany

ARTICLE INFO

Article history:
Received 9 November 2009
Received in revised form 7 January 2010
Accepted 30 January 2010
Available online 12 February 2010

MSC:
65Z05
65M60

Keywords:
Hybrid numerical methods
Finite Integration Technique
Finite Volume Method
Split operator technique
Adaptive mesh refinement

ABSTRACT

A hybridized scheme for the numerical solution of transient electromagnetic field problems is presented. The scheme combines the Finite Integration Technique (FIT) and the Finite Volume Method (FVM) in order to profit from the computational efficiency of the FIT while taking advantage of the superior dispersive properties of the FVM. The scheme is based on the longitudinal–transverse (LT) splitting of the discrete curl operator. The FIT is employed for discretizing the two-dimensional subproblem while the one-dimensional problem is discretized according to the FVM. The scheme offers benefits for the simulation of multiscale setups, where the size of the computational domain along one preferred direction is electrically much larger than along the others. In such situations, the accumulation of dispersion errors within hundreds of thousands of time steps usually deteriorates the solution accuracy. The hybrid scheme is applied in combination with adaptive mesh refinement, yielding an efficient scheme for multiscale applications.

1. Introduction

The development of a hybrid numerical method is motivated from the idea of combining the strengths of different existing methods. One appealing feature of the Finite Integration Technique (FIT) is the preservation of the physical properties of Maxwell's equations in the discrete space, e.g. energy conservation [1,2]. The simplicity of the FIT leads to a computationally inexpensive algorithm, requiring a minimum of computer memory and computational time. Finite Volume Methods (FVM), on the other hand, are known for their low numerical dispersion [3]. They are traditionally applied to problems from fluid dynamics, where the accurate simulation of shocks and turbulences critically depends on small dispersion errors. However, the FVM is computationally more expensive than the FIT. The main idea of a hybrid Finite Integration–Finite Volume Scheme is, hence, to combine the computational efficiency of the FIT with the FVM such that improved dispersion properties emerge along one direction in space. This hybrid scheme offers benefits for the simulation of wave propagation in all applications exhibiting a preferred direction. Such applications frequently occur, e.g. when simulating waveguides, strip lines, or optical fibers. In addition, the simulation of linear particle accelerators forms a class of multi-physics problems, suitable for the application of the hybrid scheme.

The superior dispersive behavior of the FVM compared to the FIT is illustrated in a simple example. The propagation of a trapezoidal wave packet in the one-dimensional space is simulated using a low spatial resolution. The initial state of the

* Corresponding author.
E-mail addresses: schnepp@gsc.tu-darmstadt.de (S. Schnepp), gjonaj@temf.tu-darmstadt.de (E. Gjonaj), weiland@temf.tu-darmstadt.de (T. Weiland).

[1] The work of S. Schnepp is supported by the 'Initiative for Excellence' of the German Federal and State Governments and the Graduate School of Computational Engineering at Technische Universität Darmstadt.

0021-9991/$ - see front matter © 2010 Elsevier Inc. All rights reserved.
doi:10.1016/j.jcp.2010.01.041

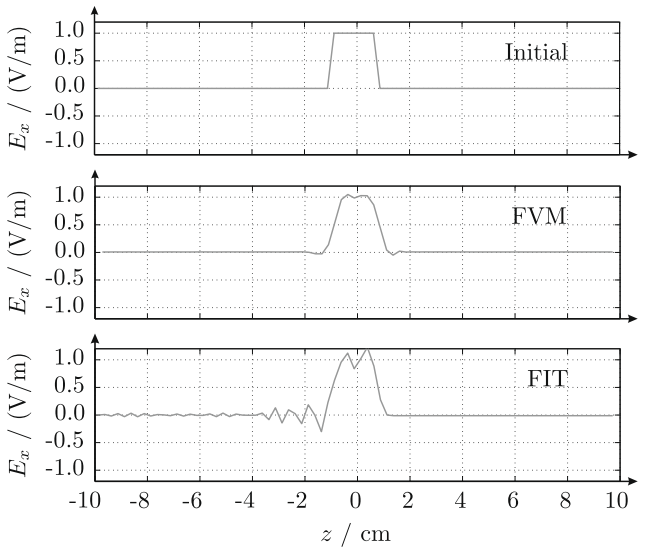

Fig. 1. Simulation of a rectangular wave packet with the FIT and the FVM. The initial field distribution is imposed on a very coarse grid (top). The length of the wave packet covers six cells and propagates in positive z-direction. The simulations employ identical grid spacings. The middle (FVM) and bottom (FIT) plots show the final distribution of the electric field after 160 time steps. The superior numerical dispersion behavior of the FVM compared to the FIT is visible.

packet is plotted in Fig. 1 (top). The orientations of the electric and magnetic field are chosen such that the wave vector $\vec{k}$ points in the positive z-direction. For the simulation, the FIT and the FVM using the same spatial grid resolution are applied. In the FVM case, the Fromm approach is applied (see Section 3). The results are illustrated in the middle (FVM) and bottom graph (FIT) of Fig. 1. The better dispersion properties make FV methods an appropriate choice for handling high-frequency fields in electrically long structures.

The remainder of this article is organized as follows: the semi-discrete formulation of the Finite Integration Technique and the Finite Volume Method are reviewed in Sections 2 and 3. For the FIT the discretization procedure in the three-dimensional space is described. Since the FVM is applied along one space dimension only, its review is limited to the one-dimensional case. The numerical fluxes considered are the Godunov, Lax-Wendroff, and Fromm flux, as well as the central flux. In Section 4, a von Neumann analysis is carried out for all semi-discrete formulations in order to derive their dispersion and dissipation properties. The hybridization of the two methods is described in detail in Section 5, followed by the introduction of the longitudinal–transverse split operator technique in Section 6. After discretizing the time variable, the dispersion and dissipation properties of the fully discretized method are investigated. This is followed by some illustrative examples and conclusions. Note that throughout the article linear, isotropic, lossless and non-polarized media are considered.

2. Semi-discrete formulation of the Finite Integration Technique

The Finite Integration Technique makes use of a pair of dual orthogonal grids $(G, \widetilde{G})$ for the spatial discretization of Maxwell's equations [4]. Throughout this article regular Cartesian grids are considered. The number of grid points along the axes are denoted by N_x, N_y and N_z. The sets of edges and faces of the primary and secondary grid are denoted by $\mathbb{E}$, $\mathbb{A}$ and $\widetilde{\mathbb{E}}$, $\widetilde{\mathbb{A}}$, respectively. The degrees of freedom (DoF) are the electric and magnetic integral state variables $\widehat{e}$ and $\widehat{h}$, which are defined as

$$\widehat{e} := \int_c \vec{E} \cdot d\vec{s}, \quad c \in \mathbb{E}, \tag{1}$$

$$\widehat{h} := \int_{\tilde{c}} \vec{H} \cdot d\vec{s}, \quad \tilde{c} \in \widetilde{\mathbb{E}}. \tag{2}$$

They are named the electric and magnetic grid voltages. The electric field is denoted by $\vec{E}$ and the magnetic field by $\vec{H}$. As a convention, we use capital letters for the space-continuous field quantities and lower case letters for space-discrete quantities.

Evaluating Faraday's and Ampére 's laws

$$\int_{\partial A} \vec{E}(\vec{r}, t) \cdot d\vec{s} = -\int_A \frac{\partial}{\partial t} \vec{B}(\vec{r}, t) \cdot d\vec{A}, \quad A \in \mathbb{A}, \tag{3}$$

$$\int_{\partial \tilde{A}} \vec{H}(\vec{r}, t) \cdot d\vec{s} = \int_{\tilde{A}} \left(\frac{\partial}{\partial t} \vec{D}(\vec{r}, t) + \vec{J}(\vec{r}, t) \right) \cdot d\vec{A}, \quad \tilde{A} \in \widetilde{\mathbb{A}}, \tag{4}$$

for one face of a primary grid cell and one face of a dual grid cell yields their local semi-discrete FIT formulations

$$\sum_{j=1}^{4} \pm \widehat{e}(j) = \pm \frac{\mathrm{d}}{\mathrm{d}t} \widehat{\widehat{b}}, \tag{5}$$

$$\sum_{j=1}^{4} \pm \widehat{h}(j) = \frac{\mathrm{d}}{\mathrm{d}t} \widehat{\widehat{d}} + \widehat{\widehat{j}}, \tag{6}$$

where j numbers the four edges of the face. The orientation of the involved voltages $\widehat{e}(j)$, $\widehat{h}(j)$ with respect to the orientation of the loop integral in (3) and (4) determines the summation signs appearing in (5) and (6). The electric and magnetic integral fluxes $\widehat{\widehat{d}}$ and $\widehat{\widehat{b}}$ are no additional degrees of freedom. They are defined as

$$\widehat{\widehat{d}} := \int_{\tilde{A}} \vec{D} \cdot \mathrm{d}\vec{A}, \quad \tilde{A} \in \tilde{\mathbb{A}}, \tag{7}$$

$$\widehat{\widehat{b}} := \int_{A} \vec{B} \cdot \mathrm{d}\vec{A}, \quad A \in \mathbb{A}, \tag{8}$$

and relate to the respective voltage according to

$$\widehat{\widehat{d}} = M_\epsilon \widehat{e}, \quad \widehat{\widehat{b}} = M_\mu \widehat{h}, \tag{9}$$

where M_ϵ and M_μ are suitably averaged discrete material parameters [5] and ϵ, μ denote the permittivity and permeability. The integral state variable of the current flux j is defined as

$$\widehat{\widehat{j}} := \int_{\tilde{A}} \vec{J} \cdot \mathrm{d}\vec{A}, \quad \tilde{A} \in \tilde{\mathbb{A}}. \tag{10}$$

Convective currents, e.g. arising from the motion of free charged particles are included in $\widehat{\widehat{j}}$.

Gathering the electric and magnetic voltages in the vectors of DoF, $\widehat{\mathbf{e}}$ and $\widehat{\mathbf{h}}$, allows for stating the discrete Faraday's and Ampére 's law for the complete computational domain in semi-discrete form

$$\mathbf{C}\widehat{\mathbf{e}} = -\mathbf{M}_\mu \frac{\mathrm{d}}{\mathrm{d}t} \widehat{\mathbf{h}}, \tag{11}$$

$$\widetilde{\mathbf{C}}\widehat{\mathbf{h}} = \mathbf{M}_\epsilon \frac{\mathrm{d}}{\mathrm{d}t} \widehat{\mathbf{e}} + \widehat{\widehat{\mathbf{j}}}. \tag{12}$$

The matrices $\mathbf{M}_\epsilon = \mathrm{diag}(M_\epsilon)$ and $\mathbf{M}_\mu = \mathrm{diag}(M_\mu)$ contain the cell-wise defined material parameters. The FIT representations of the curl operator $\mathbf{C}$ and $\widetilde{\mathbf{C}}$ resemble the structure of the continuous curl operator

$$\mathbf{C} = \begin{pmatrix} \mathbf{0} & -\mathbf{P}_z & \mathbf{P}_y \\ \mathbf{P}_z & \mathbf{0} & -\mathbf{P}_x \\ -\mathbf{P}_y & \mathbf{P}_x & \mathbf{0} \end{pmatrix}, \tag{13}$$

where the block matrices $\mathbf{P}$ are discrete derivative operators [5]. Substituting

$$\widehat{\mathbf{e}}' = \mathbf{M}_\epsilon^{1/2} \widehat{\mathbf{e}}, \quad \widehat{\mathbf{h}}' = \mathbf{M}_\mu^{-1/2} \widehat{\mathbf{h}} \tag{14}$$

and using the relation $\mathbf{C} = \widetilde{\mathbf{C}}^{\mathrm{T}}$, (11) and (12) can be written as a system of ordinary differential equations (ODE) of the form

$$\frac{\mathrm{d}}{\mathrm{d}t} \begin{pmatrix} \widehat{\mathbf{e}}' \\ \widehat{\mathbf{h}}' \end{pmatrix} = \underbrace{\begin{pmatrix} \mathbf{0} & \mathbf{M}_\epsilon^{-1/2} \mathbf{C}^{\mathrm{T}} \mathbf{M}_\mu^{-1/2} \\ -\mathbf{M}_\mu^{-1/2} \mathbf{C} \mathbf{M}_\epsilon^{-1/2} & \mathbf{0} \end{pmatrix}}_{\mathbf{A}_{\mathrm{FIT}}} \begin{pmatrix} \widehat{\mathbf{e}}' \\ \widehat{\mathbf{h}}' \end{pmatrix} - \begin{pmatrix} \mathbf{M}_\epsilon^{-1/2} \widehat{\mathbf{j}} \\ \mathbf{0} \end{pmatrix}. \tag{15}$$

Since $\mathbf{A}_{\mathrm{FIT}}$ is a skew-symmetric matrix its eigenvalues are either zero or pairwise conjugate imaginary. The semi-discrete FIT equations preserve the Hamiltonian structure of the Maxwell's equations in continuum. This guarantees the method to preserve the electromagnetic energy [6].

3. Semi-discrete formulation of the Finite Volume Method

The Finite Volume Method is derived from Faraday's and Ampére 's law in conservative form. This is considered in the one-dimensional case using the z-coordinate only and, for simplicity, neglecting current sources

$$\frac{\partial}{\partial t} \vec{U} + \frac{\partial}{\partial z} \mathbf{F}(\vec{U}) = 0, \quad \vec{U} = \begin{pmatrix} \epsilon \vec{E}^{1\mathrm{D}} \\ \mu \vec{H}^{1\mathrm{D}} \end{pmatrix}, \tag{16}$$

with $\vec{E}^{1D} = (E_x, E_y)^T$ and $\vec{H}^{1D} = (H_x, H_y)^T$. The flux function F is given by

$$F(\dot{U}) = (-H_y, H_x, E_y, -E_x)^T. \tag{17}$$

Integrating (16) over a finite interval in space yields

$$\frac{d}{dt}\int_{\Delta z} \dot{U}\, dz + \int_{\Delta z} \frac{\partial}{\partial z} F(\dot{U})\, dz = 0. \tag{18}$$

The value of $\dot{U}$ at the interval endpoints is denoted by $\dot{U}^{\square}$. The DoF in the framework of Finite Volume Methods are integral state variables given by

$$\mathbf{u}(i_z) := \frac{1}{\Delta z(i_z)} \int_{\Delta z(i_z)} \dot{U}\, dz, \tag{19}$$

and

$$\mathbf{u}(i_z) = (\epsilon e_x(i_z), \epsilon e_y(i_z), \mu h_x(i_z), \mu h_y(i_z))^T. \tag{20}$$

The width of the interval $i_z \in \{1..N_z\}$ is denoted by $\Delta z(i_z)$ and $\mathbf{u}(i_z)$ is the local vector of the DoF. Inserting this into (18) and applying the divergence theorem yields the local, semi-discrete FV formulation

$$\frac{d}{dt}\mathbf{u}(i_z) + \frac{1}{\Delta z(i_z)}\left[F\left(\dot{U}^{\square}(i_z)^{\wedge}\right) - F\left(\dot{U}^{\square}(i_z)^{-}\right)\right] = 0, \tag{21}$$

with $\dot{U}^{\square}(i_z)^{\wedge/-}$ located at the upper and lower interval endpoint

$$z(i_z)^{\wedge/-} = z(i_z) + / - \frac{\Delta z(i_z)}{2}, \tag{22}$$

where $z(i_z)$ is the interval midpoint. Hence, the temporal change of the electromagnetic quantities in the interval equals the sum of the boundary fluxes $F^j(\dot{U}^{\square})$.

Due to the definition of the DoF given in (19), the values on interval boundaries are ambiguous. There exist the two values, $\dot{U}^{\square}$ and $\dot{U}^{+}$, referring to the interior and exterior side of the boundary. Two options [7,8] for obtaining effective interface field values $e^{\square}$, $h^{\square}$ consist in the central flux approximation

$$\begin{aligned} e_x^{\square} &:= \tfrac{1}{2}(E_x^{+} + E_x^{\square}), \quad h_x^{\square} := \tfrac{1}{2}(H_x^{+} + H_x^{\square}), \\ e_y^{\square} &:= \tfrac{1}{2}\left(E_y^{+} + E_y^{\square}\right), \quad h_y^{\square} := \tfrac{1}{2}\left(H_y^{+} + H_y^{\square}\right), \end{aligned} \tag{23}$$

and the upwind flux approximation

$$\begin{aligned} e_x^{\square} &:= \frac{\left(Y^{+}E_x^{+} - H_y^{+}\right) + \left(Y^{\square}E_x^{\square} + H_y^{\square}\right)}{Y^{+} + Y^{\square}}, \\ h_x^{\square} &:= \frac{\left(Z^{+}H_x^{+} + E_y^{+}\right) + \left(Z^{\square}H_x^{\square} - E_y^{\square}\right)}{Z^{+} + Z^{\square}}, \\ e_y^{\square} &:= \frac{\left(Y^{+}E_y^{+} + H_x^{+}\right) + \left(Y^{\square}E_y^{\square} - H_x^{\square}\right)}{Y^{+} + Y^{\square}}, \\ h_y^{\square} &:= \frac{\left(Z^{+}H_y^{+} - E_x^{+}\right) + \left(Z^{\square}H_y^{\square} + E_x^{\square}\right)}{Z^{+} + Z^{\square}}, \end{aligned} \tag{24}$$

with

$$Z^{\square} := \sqrt{\frac{\epsilon^{\square}}{\mu^{\square}}} \quad \text{and} \quad Y^{\square} := \frac{1}{Z^{\square}}. \tag{25}$$

The upwind values are the exact solution of the Riemann problem for Maxwell's equations with piecewise constant initial data after an infinitesimal time span [8].

The values on the positive and negative side of the interval boundary are reconstructed from the electromagnetic field within the interval i_z applying the linear ansatz

$$E_x(i_z, z) = e_x(i_z) + (z - z(i_z))\, s(e_x) \tag{26}$$

for the E_x component and likewise for all other components. The slope s is an approximation of arbitrary order to the derivative, e.g.

$$s(e_x) \approx \frac{\partial}{\partial z} E_x. \tag{27}$$

Different FV methods use different slope definitions. In Godunov's method, it is chosen as

$$s^{G}(e_x) := 0 \tag{28}$$

yielding a piecewise constant reconstruction within every cell. Other methods use the volume average in neighboring cells to construct the slope. For the Lax-Wendroff scheme, the slope reads

$$s^{LW}(e_x) := \begin{cases} \frac{e_x(i_z) - e_x(i_z - 1)}{z(i_z) - z(i_z - 1)}, & z > z(i_z), \\ \frac{e_x(i_z + 1) - e_x(i_z)}{z(i_z + 1) - z(i_z)}, & z < z(i_z). \end{cases} \tag{29}$$

In Fromm's scheme, central differences are used for the approximation

$$s^{F}(e_x) := \frac{e_x(i_z + 1) - e_x(i_z - 1)}{z(i_z + 1) - z(i_z - 1)}. \tag{30}$$

Given one of these slope approximations, the reconstructed boundary values of E_x are obtained by

$$E_x^{\pm}(i_z) = e_x(i_z) + / - \frac{\Delta z(i_z)}{2} s(e_x). \tag{31}$$

All other components are evaluated analogously.

Arranging the semi-discrete FV formulation in the form of a system of ODEs yields (cf. (15))

$$\frac{\mathrm{d}}{\mathrm{d}t}\begin{pmatrix} \mathbf{e} \\ \mathbf{h} \end{pmatrix} = \mathbf{A}_{\mathrm{FVM}} \begin{pmatrix} \mathbf{e} \\ \mathbf{h} \end{pmatrix}, \tag{32}$$

with the vectors of DoF $\mathbf{e}$ and $\mathbf{h}$. The system matrix employing central fluxes reads

$$\mathbf{A}_{\mathrm{FVM}}^{\mathrm{cen}} = \begin{pmatrix} \mathbf{0} & \mathbf{0} & \mathbf{0} & \mathbf{D}_{\epsilon}^{-1}\mathbf{P}_z \\ \mathbf{0} & \mathbf{0} & -\mathbf{D}_{\epsilon}^{-1}\mathbf{P}_z & \mathbf{0} \\ \mathbf{0} & \mathbf{D}_{\mu}^{-1}\mathbf{P}_z & \mathbf{0} & \mathbf{0} \\ -\mathbf{D}_{\mu}^{-1}\mathbf{P}_z & \mathbf{0} & \mathbf{0} & \mathbf{0} \end{pmatrix}, \tag{33}$$

where the block matrix $\mathbf{P}_z$ is the discrete FV derivative operator and $\mathbf{D}_{\mu} = \mathrm{diag}(\mu(i_z))$, $\mathbf{D}_{\epsilon} = \mathrm{diag}(\epsilon(i_z))$ are the material matrices. It allows for identifying the discrete FV curl operator $\mathbf{C}$ for the considered one-dimensional case

$$\mathbf{C} = \begin{pmatrix} \mathbf{0} & -\mathbf{P}_z \\ \mathbf{P}_z & \mathbf{0} \end{pmatrix}. \tag{34}$$

Using the substitutions (14) the system matrix of the central flux FVM reveals a skew-symmetric form. It is formally identical to the FIT system matrix and exhibits pairwise conjugate imaginary eigenvalues.

In the case of the upwind flux formulation, the system matrix reads

$$\mathbf{A}_{\mathrm{FVM}}^{\mathrm{up}} = \begin{pmatrix} \mathbf{U}_e & \mathbf{0} & \mathbf{0} & \mathbf{D}_{\epsilon}^{-1}\mathbf{P}_z \\ \mathbf{0} & \mathbf{U}_e & -\mathbf{D}_{\epsilon}^{-1}\mathbf{P}_z & \mathbf{0} \\ \mathbf{0} & \mathbf{D}_{\mu}^{-1}\mathbf{P}_z & \mathbf{U}_h & \mathbf{0} \\ -\mathbf{D}_{\mu}^{-1}\mathbf{P}_z & \mathbf{0} & \mathbf{0} & \mathbf{U}_h \end{pmatrix} \tag{35}$$

with the upwind operators $\mathbf{U}_e$ and $\mathbf{U}_h$. This matrix is no longer skew-symmetric. Its eigenvalues are either zero or pairwise conjugate complex.

4. Properties of the semi-discrete FIT and FVM

The two methods introduced above are investigated for their dispersion and dissipation properties by means of a von Neumann analysis [3]. This analysis assumes an infinite grid of identical cells. It is, hence, sufficient to consider one representative cell. For a plane wave solution

$$\widehat{e} = \mathrm{e}^{\mathrm{i}(\omega t - \vec{k}\cdot\vec{r})} \tag{36}$$

the DoF of neighboring cells are obtained by the multiplication with a phase factor, e.g.

$$\widehat{e}_x(i_z + 1) = \widehat{e}_x(i_z)\,\mathrm{e}^{-\mathrm{i}k_z\Delta z} \tag{37}$$

for the x-directed FIT electric voltage in the neighboring cell along the positive z-direction. This allows for establishing a local eigenvalue equation. For the FIT its solutions λ_A are real-valued. The corresponding dispersion relation reads [9]

$$\sum_u \left[\left(\frac{\sin\left(\frac{k_u \Delta u}{2}\right)}{\frac{\Delta u}{2}} \right)^2 \right] = \left(\frac{\omega}{c}\right)^2 \quad \text{with } u \in \{x, y, z\}. \tag{38}$$

If the plane waves are assumed to propagate along an axis of the coordinate system, e.g. the z-axis, all but one term of the sum are equal to zero. Then, the relation reduces to

$$2 \sin\left(\frac{k_z \Delta z}{2}\right) = \Delta z \frac{\omega}{c}. \tag{39}$$

In Fig. 2 the normalized angular frequency is plotted as a function of the phase advance per cell, β, along the coordinate z

$$\beta := k_z \Delta z. \tag{40}$$

The graph shows that all discrete waves lag behind their continuous counterpart independently of the grid resolution. In the long wave limit ($\beta \to 0$), the physical phase speed is recovered.

For the upwind formulation of the FVM the local eigenvalue problem has complex solutions $\lambda_A \in \mathbb{C}$. The dispersion relation can be written in the general form

$$\Phi(k\Delta z) \cdot A(k\Delta z) = \Delta z \frac{\omega}{c}, \tag{41}$$

with the phase function Φ and the amplification function A

$$\Phi(k\Delta z) = e^{i\mathrm{Re}\{\lambda_A\}}, \tag{42}$$

$$A(k\Delta z) = e^{-\Im\{\lambda_A\}}. \tag{43}$$

For the slope definitions given in Eqs. (28)–(30), they read

- Godunov:

$$\Phi^G(k\Delta z) = \sin(k\Delta z), \tag{44}$$

$$A^G(k\Delta z) = \exp(\cos(k\Delta z) - 1), \tag{45}$$

- Lax-Wendroff:

$$\Phi^{LW}(k\Delta z) = (2 - \cos(k\Delta z)) \sin(k\Delta z), \tag{46}$$

$$A^{LW}(k\Delta z) = \exp\left(4 \cdot \sin^4\left(\frac{k\Delta z}{2}\right)\right), \tag{47}$$

- Fromm:

$$\Phi^F(k\Delta z) = \left(\frac{3 - \cos(k\Delta z)}{2}\right) \sin(k\Delta z), \tag{48}$$

$$A^F(k\Delta z) = \exp\left(2 \cdot \sin^4\left(\frac{k\Delta z}{2}\right)\right). \tag{49}$$

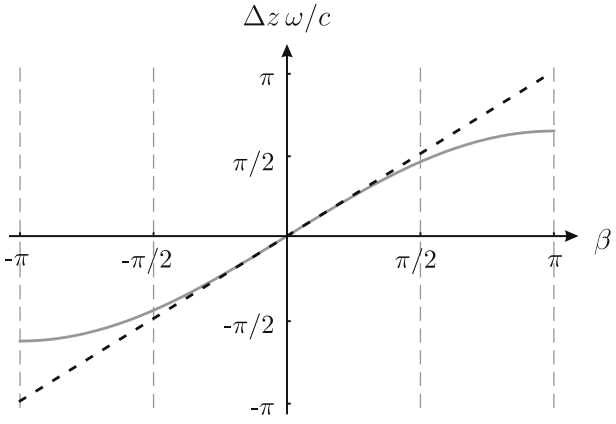

Fig. 2. The plot shows the numerical phase advance of plane waves in the grid space traveling along the z-axis in comparison to the phase advance in continuous space (dashed line). Discrete waves of all frequencies show a phase lag in comparison to the continuous case. In the long wave limit ($\beta \to 0$) the physical phase velocity is recovered.

Comparing the semi-discrete dispersion relations of the FIT (39) and Godunov's method (44), it is evident that Godunov's method requires twice the grid resolution in order to yield the same phase accuracy. This is a direct consequence of the staggered pair of grids employed by the FIT. In Fig. 3 the dispersion graphs and dissipation graphs are shown. Instead of the amplification, the damping $\delta 1 - A\rangle$ is plotted. From these graphs it can be concluded that Fromm's method has the best dispersion properties. The damping increases along with β for each of the three methods. For the Lax-Wendroff and Fromm's method, however, damping is low for reasonably small values of β (cf. Table 1). In the long wave limit $\delta\beta \to 0\rangle$, the error in phase as well as the damping tend to zero for all three FVM-type methods.

With these dispersion relations at hand (Eqs. (39), (44), (46) and (48)), an expression for the error in the numerical phase advance can be established. For waves propagating along a coordinate it is given by

$$\Delta\beta = k_z \Delta z - \Phi(k\Delta z), \tag{50}$$

where the phase function Φ is taken from the dispersion relation of the respective method. This expression can be expanded into a power series about the point $\beta = 0$. This yields

$$\Delta\beta - \frac{k_z^3 \Delta z^3}{24} - \frac{k_z^5 \Delta z^5}{1920}, \tag{51}$$

in the case of the FIT. The leading term of this long wave approximation, defines the asymptotic order of the dispersion error [10]. For the three FVMs following the same procedure yields

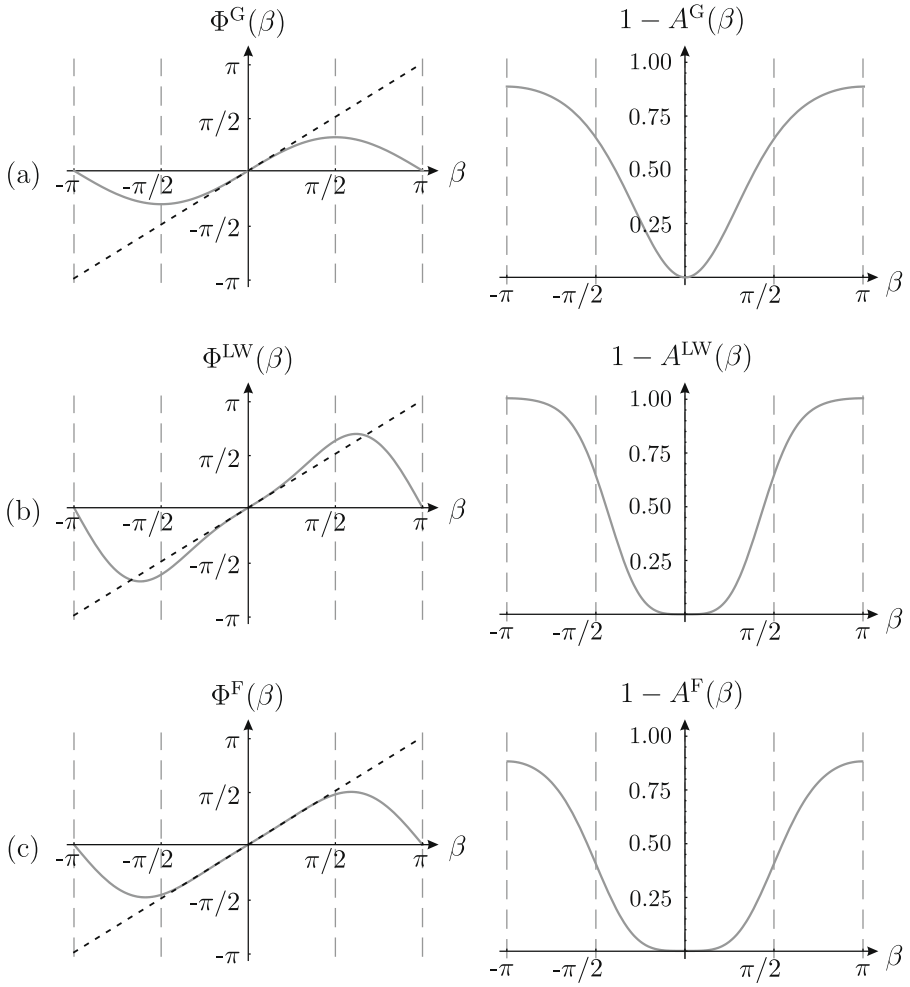

Fig. 3. Grid dispersion and dissipation diagrams for the Godunov (a), Lax-Wendroff (b) and Fromm (c) method. The plots show the numerical phase advance Φ and damping $1 - A$. For Godunov's method, analogously to the FIT, all waves in the grid space lag behind the continuous case (dashed line). However, a comparison to the dispersion relation of the FIT (see Fig. 2) reveals, that the grid resolution has to be doubled in order to yield the same result. The Lax-Wendroff and Fromm method show a phase advance or a phase lag depending on the actual β with Fromm's method clearly performing best. Dissipation increases with β for each of the three methods. For the Lax-Wendroff and Fromm's method, however, damping is low in a larger neighborhood of $\beta = 0$.

Table 1
Amplification factors for resolutions of 5, 8, 12, and 15 grid points per wavelength.

	5	8	12	15
Godunov	0.501	0.746	0.875	0.917
Lax-Wendroff	0.620	0.918	0.982	0.993
Fromm	0.788	0.958	0.991	0.996

- Godunov:

$$\Delta\beta = \frac{k_z^3 \Delta z^3}{6} + \frac{k_z^5 \Delta z^5}{120}, \tag{52}$$

- Lax-Wendroff:

$$\Delta\beta = -\frac{k_z^3 \Delta z^3}{3} + \frac{7 k_z^5 \Delta z^5}{60}, \tag{53}$$

- Fromm:

$$\Delta\beta = -\frac{k_z^3 \Delta z^3}{12} + \frac{13 k_z^5 \Delta z^5}{240}. \tag{54}$$

The dominant error term is of the order three. All schemes are, thus, second order accurate in the long wave limit $(\beta \to 0)$ with respect to numerical dispersion errors (see Fig. 4 for an illustration).

A similar expansion can be done for the dissipation error of the FVMs (Eqs. (45), (47) and (49)). It reveals that Godunov's method is first order accurate and the Lax-Wendroff and Fromm scheme are third order accurate with respect to numerical dissipation errors.

The above expressions for the asymptotic orders of the dispersion error do not explain the better dispersion behavior of Fromm's method, which was observed in Fig. 1. Since a wave packet was considered there, also the group velocity has to be investigated. To this end, we differentiate the phase functions (39), (44), (46) and (48) with respect to k. In Fig. 5 the numerical group velocities v_g are plotted. There, and for the remainder of this article, the curves are plotted within $\beta = [-\pi/2, \pi/2]$ only. Since the spectrum is actually not continuous but discrete with $\beta = \{\pi/n_z,\ n_z = 1..N_z\}$, only the mode at $\beta = -\pi$ is neglected in the plots. For the FV methods this mode does not propagate (see Fig. 3). Averaging v_g in $[-\pi/2, \pi/2]$ yields mean group velocities for all methods, which are listed in the center column of Table 2. The average group velocity of Fromm's method is closest to the speed of light in continuum. Hence, it will usually preserve the envelope of a wave packet best.

Additionally, the error in normalized phase velocity of every discrete mode can be evaluated as

$$\mathsf{E}_{n_z} = \frac{\pi}{n_z} - \Phi\left(\frac{\pi}{n_z}\right). \tag{55}$$

The errors are gathered in the vector E. Its 2-norm is given in the right column of Table 2 for $N_z = 100$. This measure as well as the mean group velocity confirm the overall better dispersion behavior of Fromm's method in comparison to the FIT, which we observed in the introductory example in Fig. 1.

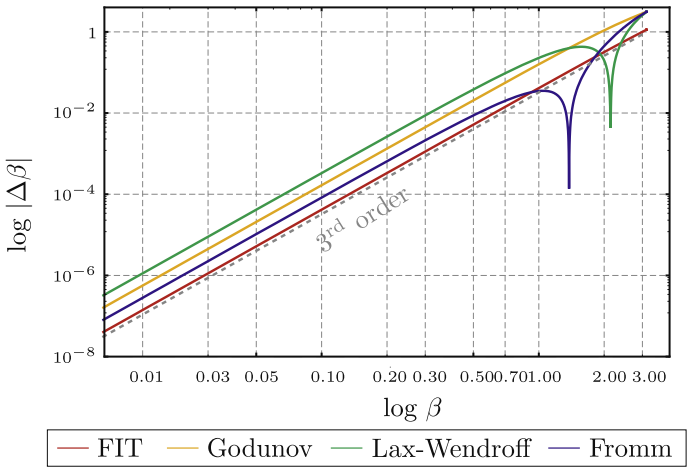

Fig. 4. Dispersion error of the FIT and FVMs: In the long wave limit of $\beta \to 0$ the dispersion error of all methods tend to zero in third order.

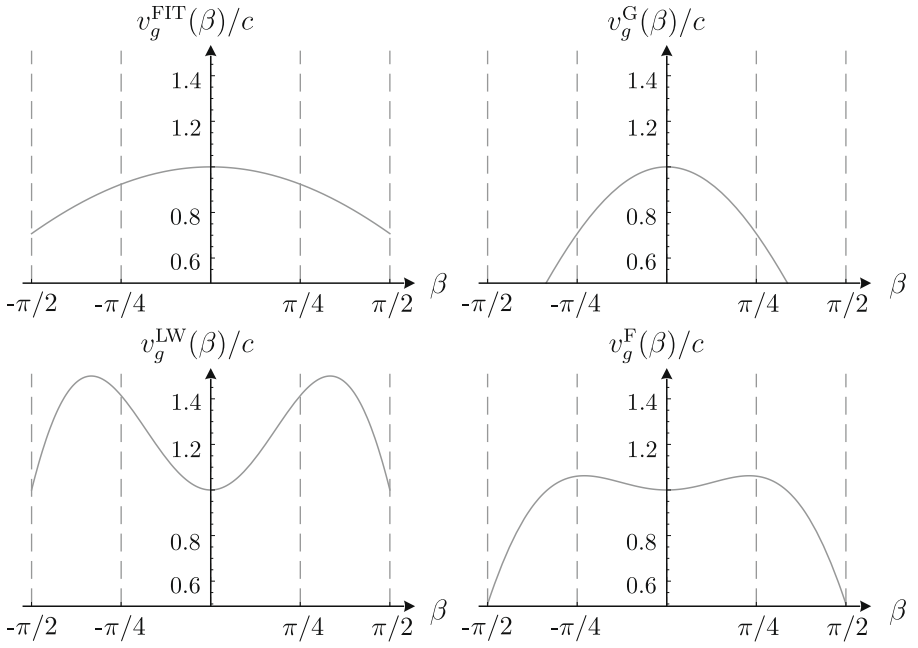

Fig. 5. Plots of the normalized group velocity for the FIT (top left), Godunov (top right), Lax-Wendroff (bottom left) and Fromm (bottom right) method.

Table 2
Normalized mean group velocities and 2-norm of normalized phase velocity errors for all methods considered.

Method	v_g/c	$\|E\|_2$
FIT	0.90	0.17
Godunov	0.63	0.61
Lax-Wendroff	1.27	0.52
Fromm	0.95	0.08

5. The three-dimensional formulation of the hybrid scheme in space

The hybridization of the Finite Integration Technique and the Finite Volume Method in three-dimensional space is based on a separation of the continuous curl operator according to

$$\mathbf{r}\times = \underbrace{\begin{pmatrix} 0 & -\frac{\partial}{\partial z} & \frac{\partial}{\partial y} \\ \frac{\partial}{\partial z} & 0 & -\frac{\partial}{\partial x} \\ -\frac{\partial}{\partial y} & \frac{\partial}{\partial x} & 0 \end{pmatrix}}_{\widehat{=}\mathbf{C}^{\mathrm{3D}}} = \underbrace{\begin{pmatrix} 0 & 0 & \frac{\partial}{\partial y} \\ 0 & 0 & -\frac{\partial}{\partial x} \\ -\frac{\partial}{\partial y} & \frac{\partial}{\partial x} & 0 \end{pmatrix}}_{\widehat{=}\mathbf{C}^{\mathrm{2D\text{-}FIT}}} + \underbrace{\begin{pmatrix} 0 & -\frac{\partial}{\partial z} & 0 \\ \frac{\partial}{\partial z} & 0 & 0 \\ 0 & 0 & 0 \end{pmatrix}}_{\widehat{=}\mathbf{C}^{\mathrm{1D\text{-}FV}}}. \tag{56}$$

The above idea of splitting the curl operator was proposed in [12]. There, however, the FIT discretization was used exclusively. This method is called LT-FIT in the following. Here, however, for the discretization of the transverse two-dimensional subproblem we want to employ the FIT, while the FVM is applied to the discretization of the longitudinal one-dimensional problem. The transverse and longitudinal directions are specified with respect to the preferred direction of the physical problem under consideration. This is illustrated in Fig. 6.

Unlike the FIT, the FVM does not employ a staggered grid doublet. The three-dimensional computational grid, thus, consists of dual orthogonal grid layers in x–y-planes which are connected in a non-staggered fashion along the z-coordinate. In Fig. 7 a detailed sketch is shown. The primary FIT grid is indicated in black, the dual in gray. The staggered FIT grid layers are arranged in the center of the cells along the z-axis. The outline of groups of four cells is indicated with black dashed boxes. Within this setup, the FVM operates along the dash-dotted z-directed lines.

5.1. Coupling of the degrees of freedom

The electric and magnetic field DoF of the FIT and FVM are defined differently. The former are integral state variables obtained by an integration over edges (Eqs. (1) and (2)). The latter are integral state variables obtained by cell averaging (19). In

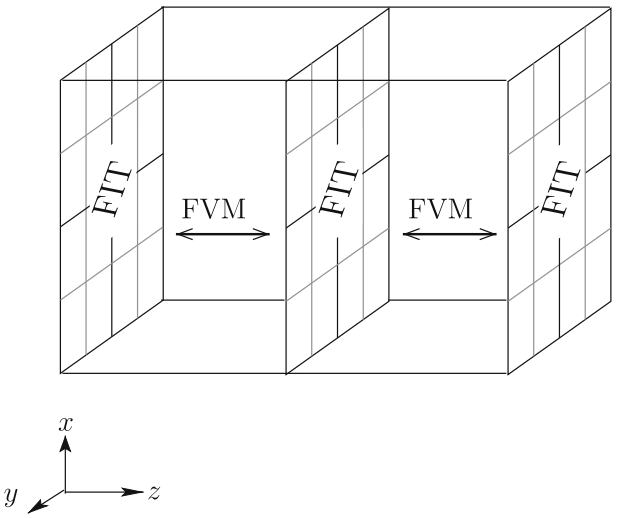

Fig. 6. Illustration of the FI–FV scheme in space. The FIT is applied in parallel x □ y-planes of the computational grid. The FVM is applied in the z-direction for connecting these planes.

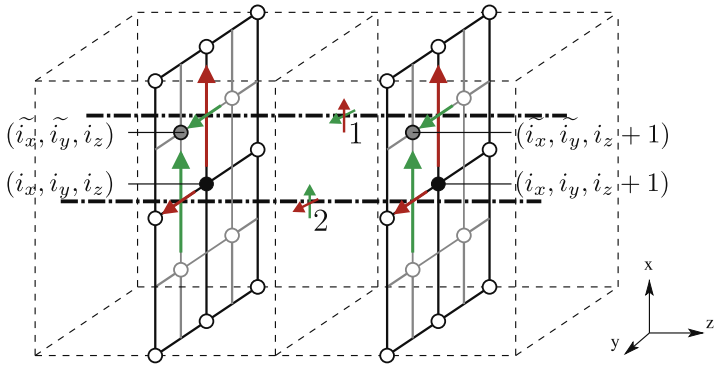

Fig. 7. FI–FV grid setup and coupling of DoFs. The FIT is applied in x □ y-planes. There, staggered grid doublets are employed. The x- and y-directed electric voltages of two grid points are shown in red, the respective magnetic voltages in green. In the z-direction, the FVM is applied, which requires one grid only. The x □ y-layers are positioned in the center of the cells in z-direction. The FVM operates along the indicated dash-dotted lines. The points 1 and 2 depict the positions where the numerical boundary fluxes are evaluated.

the following, their coupling is addressed. In Fig. 7, two primary and the respective dual nodes, marked as dots, are indexed by (i_x, i_y, i_z) and $(i_x, i_y, i_z + 1)$. The red arrows indicate the electric grid voltages $\widehat{e}_x(i_x, i_y, i_z)$, $\widehat{e}_y(i_x, i_y, i_z)$ and $\widehat{e}_x(i_x, i_y, i_z + 1)$, $\widehat{e}_y(i_x, i_y, i_z + 1)$. The green arrows indicate the respective magnetic voltages $h_x(\widetilde{i_x}, \widetilde{i_y}, i_z)$, $h_y(\widetilde{i_x}, \widetilde{i_y}, i_z)$ and $h_x(\widetilde{i_x}, \widetilde{i_y}, i_z + 1)$, $h_y(\widetilde{i_x}, \widetilde{i_y}, i_z + 1)$. For simplicity, the indexes i_x and i_y are omitted in the following. The notation is, thus, $\widehat{e}_x(i_z)$, etc. for the FIT variables and $e_x(i_z)$, etc. for the FV variables.

In order to obtain a sampled field value from the FIT voltages in the middle of an edge, we calculate

$$\hat{e}_x(i_z) = \frac{\widehat{e}_x(i_z)}{\Delta x(i_z)} \tag{57}$$

for the electric x-component and likewise for all other quantities. The involved grid voltages are oriented perpendicularly to the z-axis. The value $\hat{e}_x(i_z)$ is taken to be constant along z within one cell. Then, the FV variable is obtained by

$$e_x(i_z) = \frac{1}{\Delta z(i_z)} \int_{\Delta z(i_z)} \hat{e}_x(i_z)\,\mathrm{d}z = \hat{e}_x(i_z). \tag{58}$$

The reconstruction of the field within a cell given by (26) can be written as

$$E_x(i_z, z) = \hat{e}_x(i_z)\,\delta z \quad \square \quad z(i_z)\,\delta\hat{e}_x. \tag{59}$$

This allows for calculating the values $E_x^{\square}$, $H_y^{\square}$ and $E_y^{\square}$, $H_x^{\square}$ at the FV-cell interfaces, at positions 1 and 2, as indicated in Fig. 7.

5.2. Matrix formulation

The semi-discrete formulation of the FI–FV scheme as a system of ODEs reads

$$\frac{\mathrm{d}}{\mathrm{d}t}\begin{pmatrix}\mathbf{e}\\ \mathbf{h}\end{pmatrix} = \mathbf{A}_{\mathrm{FI-FV}}\begin{pmatrix}\mathbf{e}\\ \mathbf{h}\end{pmatrix}, \tag{60}$$

where the system matrix of the three-dimensional hybrid FI–FV scheme is given by

$$\mathbf{A}_{\mathrm{FI-FV}} = \begin{pmatrix}\mathbf{U}_H & -\mathbf{C}_E\\ \mathbf{C}_H & \mathbf{U}_E\end{pmatrix}. \tag{61}$$

The block matrices are given by

$$\mathbf{U}_H = \begin{pmatrix}\mathbf{U}_h & \mathbf{0} & \mathbf{0}\\ \mathbf{0} & \mathbf{U}_h & \mathbf{0}\\ \mathbf{0} & \mathbf{0} & \mathbf{0}\end{pmatrix}, \tag{62}$$

$$\mathbf{U}_E = \begin{pmatrix}\mathbf{U}_e & \mathbf{0} & \mathbf{0}\\ \mathbf{0} & \mathbf{U}_e & \mathbf{0}\\ \mathbf{0} & \mathbf{0} & \mathbf{0}\end{pmatrix}, \tag{63}$$

$$\mathbf{C}_H = \begin{pmatrix}\mathbf{0} & -\left(\mathbf{T}_y^h\right)^{-1}\mathbf{D}_\epsilon^{-1}\mathbf{P}_z^{\mathrm{T}}\mathbf{T}_y^h & -\mathbf{M}_{\epsilon,x}^{-1}\mathbf{P}_y\\ \left(\mathbf{T}_x^h\right)^{-1}\mathbf{D}_\epsilon^{-1}\mathbf{P}_z^{\mathrm{T}}\mathbf{T}_x^h & \mathbf{0} & \mathbf{M}_{\epsilon,y}^{-1}\mathbf{P}_x\\ \mathbf{M}_{\epsilon,x}^{-1}\mathbf{P}_y & -\mathbf{M}_{\epsilon,y}^{-1}\mathbf{P}_x & \mathbf{0}\end{pmatrix}, \tag{64}$$

$$\mathbf{C}_E = \begin{pmatrix}\mathbf{0} & \left(\mathbf{T}_y^e\right)^{-1}\mathbf{D}_\mu^{-1}\mathbf{P}_z\mathbf{T}_y^e & \mathbf{M}_{\mu,x}^{-1}\mathbf{P}_y\\ -\left(\mathbf{T}_x^e\right)^{-1}\mathbf{D}_\mu^{-1}\mathbf{P}_z\mathbf{T}_x^e & \mathbf{0} & -\mathbf{M}_{\mu,y}^{-1}\mathbf{P}_x\\ -\mathbf{M}_{\mu,x}^{-1}\mathbf{P}_y & \mathbf{M}_{\mu,y}^{-1}\mathbf{P}_x & \mathbf{0}\end{pmatrix}. \tag{65}$$

The discrete derivative operators $\mathbf{P}_{x,y}$ are the respective FIT operator while $\mathbf{P}_z$ is the FV operator. The matrices $\mathbf{T}_x^e$, $\mathbf{T}_y^e$, $\mathbf{T}_x^h$ and $\mathbf{T}_y^h$ transform the FIT variables to the FV variables. They read

$$\mathbf{T}_x^e = \mathrm{diag}(\epsilon(i_x, i_y, i_z+\tfrac{1}{2}))\,\mathrm{diag}(\Delta x(i_x, i_y, i_z+\tfrac{1}{2}))^{-1}, \tag{66}$$

$$\mathbf{T}_y^e = \mathrm{diag}(\epsilon(i_x, i_y, i_z+\tfrac{1}{2}))\,\mathrm{diag}(\Delta y(i_x, i_y, i_z+\tfrac{1}{2}))^{-1}, \tag{67}$$

$$\mathbf{T}_x^h = \mathrm{diag}(\mu(i_x, i_y, i_z+\tfrac{1}{2}))\,\mathrm{diag}(\widetilde{\Delta x}(i_x, i_y, i_z+\tfrac{1}{2}))^{-1}, \tag{68}$$

$$\mathbf{T}_y^h = \mathrm{diag}(\mu(i_x, i_y, i_z+\tfrac{1}{2}))\,\mathrm{diag}(\widetilde{\Delta y}(i_x, i_y, i_z+\tfrac{1}{2}))^{-1}. \tag{69}$$

6. Time integration and longitudinal–transverse split operator method

6.1. Time integration in the central flux case

The system matrices of the FIT as well as the central flux formulation of the FVM (Eqs. (15) and (33)) exhibit a Hamiltonian structure. For the numerical integration of Hamiltonian systems symplectic integrators are widely used since they strictly conserve the volume occupied in the phase space spanned by the electric field $\vec{E}$ and the magnetic field $\vec{H}$. For linear systems, this in turn guarantees for no accumulation of the error in the total energy of the discrete solution [6] in the long term.

The simplest symplectic time integration scheme is the leap-frog scheme. It is commonly applied for the solution of transient problems with the FIT [4]. The leap-frog scheme makes use of a central difference approximation of the derivative in time. The fully discrete system of equations reads

$$\frac{\mathbf{u}^{n+1} - \mathbf{u}^n}{\Delta t} = \mathbf{A}\mathbf{u}^n, \tag{70}$$

with

$$\mathbf{u}^n = \begin{pmatrix}\mathbf{e}^{n+1/2}\\ \mathbf{h}^n\end{pmatrix}, \tag{71}$$

where Δt denotes the time step and n denotes the time step number. The system matrix $\mathbf{A}$ corresponds to (15) or (33), respectively. Arranging (70) in the form

$$\mathbf{u}^{n+1} = \mathbf{T}\mathbf{u}^n \tag{72}$$

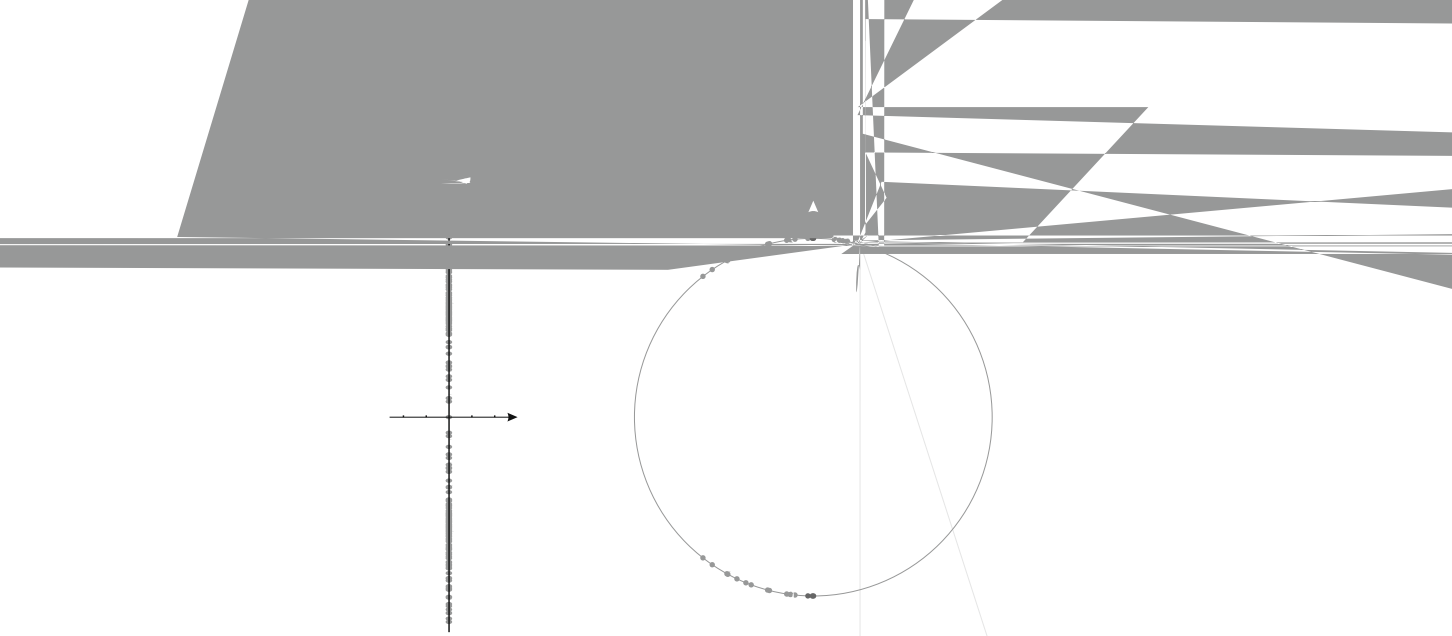

yields the update equation. The FIT iteration matrix $\mathbf{T}$ reads

$$\mathbf{T} = \begin{pmatrix} \mathbf{I} & \Delta t \mathbf{M}_{\epsilon}^{-1/2} \mathbf{C}^{\mathrm{T}} \mathbf{M}_{\mu}^{-1/2} \\ -\Delta t \mathbf{M}_{\mu}^{-1/2} \mathbf{C} \mathbf{M}_{\epsilon}^{-1/2} & \mathbf{I} - \Delta t^2 \mathbf{M}_{\epsilon}^{-1/2} \mathbf{C}^{\mathrm{T}} \mathbf{M}_{\mu}^{-1} \mathbf{C} \mathbf{M}_{\epsilon}^{-1/2} \end{pmatrix}. \tag{73}$$

The FV iteration matrix in the centered case is obtained accordingly. The symplectic property of phase space volume conservation can be expressed by the condition

$$\mathbf{T}^{\mathrm{T}} \begin{pmatrix} \mathbf{0} & \mathbf{I} \\ -\mathbf{I} & \mathbf{0} \end{pmatrix} \mathbf{T} = \begin{pmatrix} \mathbf{0} & \mathbf{I} \\ -\mathbf{I} & \mathbf{0} \end{pmatrix}, \tag{74}$$

which holds true for the iteration matrix $\mathbf{T}$ given above.

The iteration matrix $\mathbf{T}$ is determined by the system matrix $\mathbf{A}$ of the respective spatial discretization method and the time integration scheme applied. The eigenvalues of the FIT iteration matrix λ_{T} relate to those of the system matrix λ_{A} according to

$$\lambda_{\mathrm{T}} = \alpha - \sqrt{\alpha^2 - 1} \quad \text{with } \alpha = 1 + \frac{1}{2}(\Delta t \lambda_{\mathrm{A}})^2. \tag{75}$$

Within the stability limit for the time step [4], the leap-frog scheme maps the pairs of imaginary eigenvalues of the FIT or FVM central flux system matrix to the unit circle in the complex plane (Fig. 8).

6.2. Time integration in the upwind case

A symplectic time integration method cannot be applied to a system with complex eigenvalues. This is demonstrated in the following. In Fig. 9 (left) an exemplary distribution of eigenvalues of the FI–FV system matrix λ_{A} is plotted in the complex plane. If the leap-frog scheme is applied to the time integration, the relation between the eigenvalues of the system matrix and the iteration matrix is given by (75). The two parts of the relation map the pairs of eigenvalues once to the inside $\left(\alpha - \sqrt{\alpha^2 - 1}\right)$ of the unit circle and once to the outside $\left(\alpha + \sqrt{\alpha^2 - 1}\right)$. The resulting eigenvalue distribution of the iteration matrix is shown in Fig. 9 (right). Obviously eigenvalues with $|\lambda_{\mathrm{T}}| > 1$ appear, which leads to an exponential amplification of the respective mode. Consequently, the fully discrete method is unstable for any choice of the time step Δt.

Runge–Kutta-type methods (RK) [11] are viable choices for the time integration of the FI–FV scheme. The update equations for the predictor–corrector method (RK2) and the classical RK4 read

$$\mathbf{u}^{n+1} = \left(\mathbf{I} + \Delta t \mathbf{A} + \frac{(\Delta t \mathbf{A})^2}{2}\right) \mathbf{u}^n, \tag{76}$$

$$\mathbf{u}^{n+1} = \left(\mathbf{I} + \Delta t \mathbf{A} + \frac{(\Delta t \mathbf{A})^2}{2} + \frac{(\Delta t \mathbf{A})^3}{6} + \frac{(\Delta t \mathbf{A})^4}{24}\right) \mathbf{u}^n. \tag{77}$$

In Fig. 10 the eigenvalue distribution of the iteration matrices for both time integration schemes are shown. The relations of the eigenvalues of the system matrix λ_{A} and those of the iteration matrix λ_{T} read

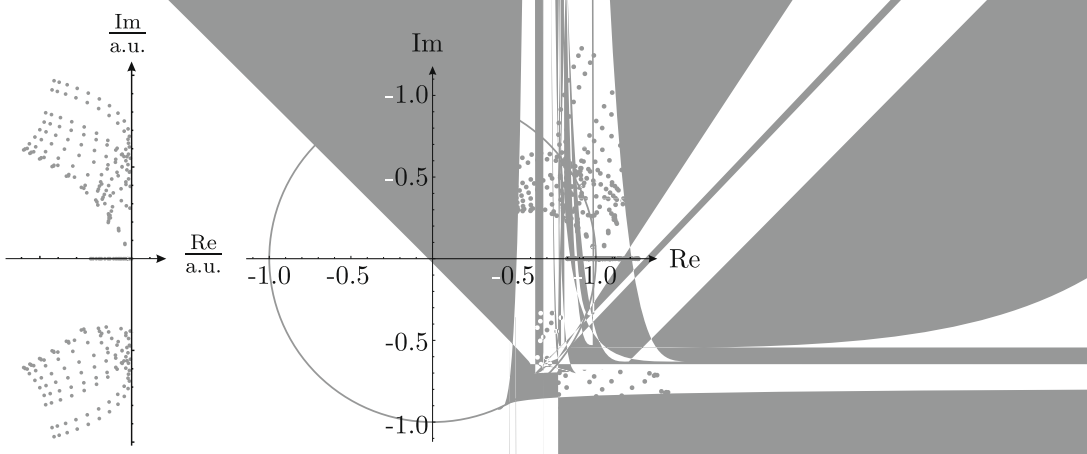

Fig. 9. Exemplary eigenvalue distribution of the FI–FV hybrid system matrix (left) and iteration matrix (right) in the complex plane. The iteration matrix results from the application of the leap-frog scheme.

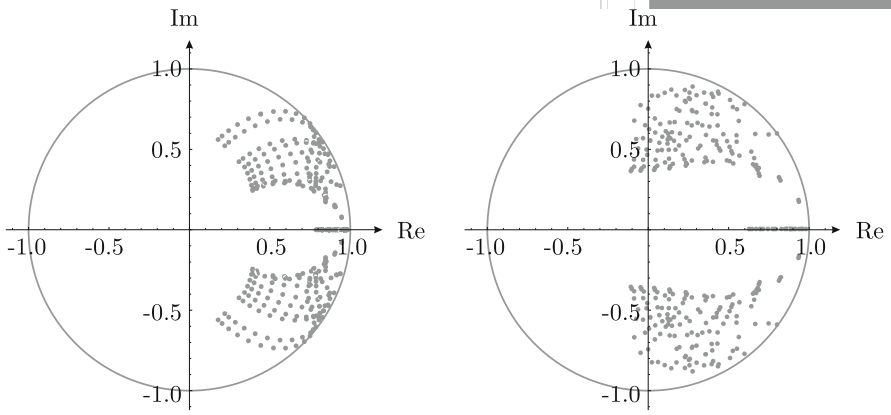

Fig. 10. Typical eigenvalue distributions of FI–FV iteration matrices resulting from Fig. 9 (left) and the application of the predictor–corrector scheme (left) and the classical Runge–Kutta-4 method (right).

$$\lambda_T = 1 + \Delta t\lambda_A + \frac{(\Delta t\lambda_A)^2}{2}\left[+\frac{(\Delta t\lambda_A)^3}{6} + \frac{(\Delta t\lambda_A)^4}{24}\right].$$

In contrast to the FIT the absolute value of the eigenvalues λ_T is in general less than
the energy of the discrete solution is preserved within the FIT.

6.3. Application of the LT split operator technique for time integration

In Section 5, a directional separation of the continuous curl operator into a two-
sional longitudinal operator was performed. In the following, the system matrix o
the form

$$\mathbf{A}_{\mathrm{FI-FV}} = \mathbf{A}_{\mathrm{FI-FV,T}} + \mathbf{A}_{\mathrm{FI-FV,L}},$$

where $\mathbf{A}_{\mathrm{FI-FV,T}}$ is the FIT discretization of the transverse problem and $\mathbf{A}_{\mathrm{FI-FV,L}}$ conta
dinal problem. The exact solution of the semi-discrete equation (60) within one t

$$\mathbf{u}^{n+1} = e^{\square\Delta t\mathbf{A}}\mathbf{u}^n = e^{\square\Delta t(\mathbf{A}_T+\mathbf{A}_L)}\mathbf{u}^n,$$

where the FI–FV subscripts were omitted. The update operator can be separated

$$e^{\square\Delta t\mathbf{A}} = e^{\square\Delta t(\mathbf{A}_T+\mathbf{A}_L)} = e^{\square\Delta t\mathbf{A}_T}\,e^{\square\Delta t\mathbf{A}_L} + O(\Delta t^2).$$

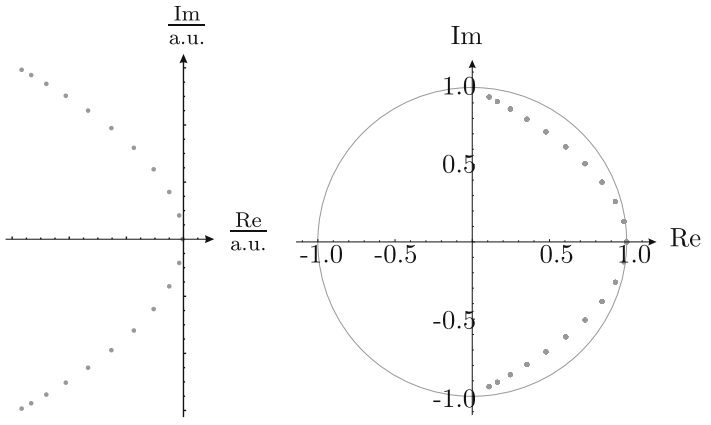

Fig. 12. Exemplary eigenvalue distribution of the longitudinal system matrix $\mathbf{A}_L$ (left) and the iteration matrix $\mathbf{T}_L$ for an application of the explicit Euler scheme (right).

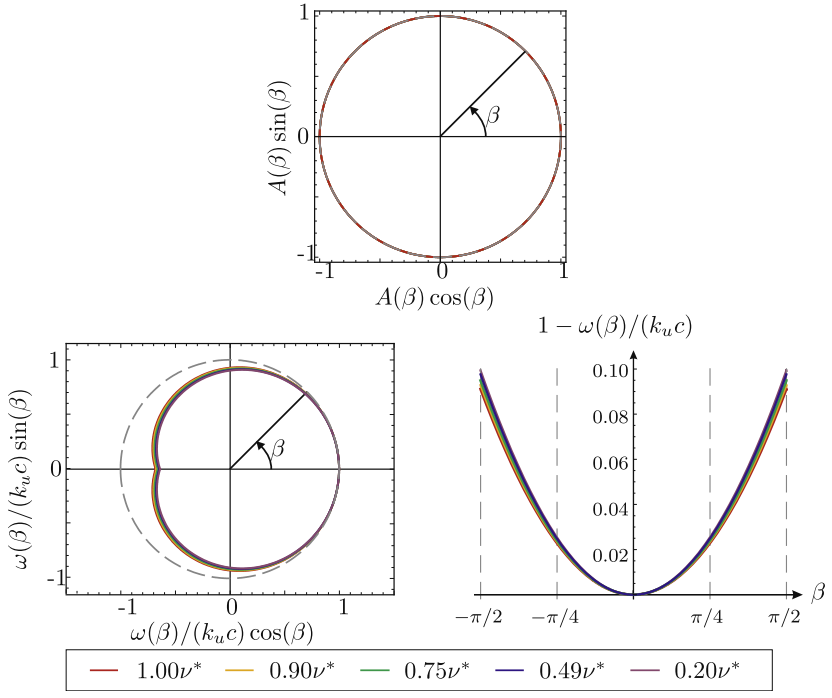

Fig. 13. Polar plots of the amplification (top), the normalized angular frequency (bottom left), and the frequency error (bottom right) of the FIT for waves traveling along a coordinate in a two-dimensional domain. The gray dashed unit circle indicates the exact solution. The curves correspond to various time steps with respect to the maximally stable CFL number ν^* for two-dimensional problems, which relates to ν by $\nu^* = \nu/\sqrt{2}$. The amplification plot shows the neutral stability for any choice of the time step within the stable regime.

where the temporal derivative of e_x was replaced by the spatial derivative of h_y according to Ampére 's law in one dimension. The spatial derivative is replaced by one of the slope approximation specified in (28)–(30)

$$\delta E_x \delta i_z)^{n+1/2} = e_x \delta i_z)^n + \frac{\Delta z}{2} s \delta e_x) - \frac{\Delta t}{2}\frac{1}{\epsilon} s \delta h_y). \tag{89}$$

The iteration matrix for the longitudinal problem $\mathbf{T}_L$ is given by

$$\mathbf{T}_L \delta \Delta t) = \mathbf{I} + \Delta t \mathbf{A}_L, \tag{90}$$

so that the eigenvalues of $\mathbf{A}_L$ and $\mathbf{T}_L$ relate according to

$$\lambda_T = 1 + \Delta t \lambda_A. \tag{91}$$

Exemplary eigenvalue distributions of both matrices are plotted in Fig. 12.

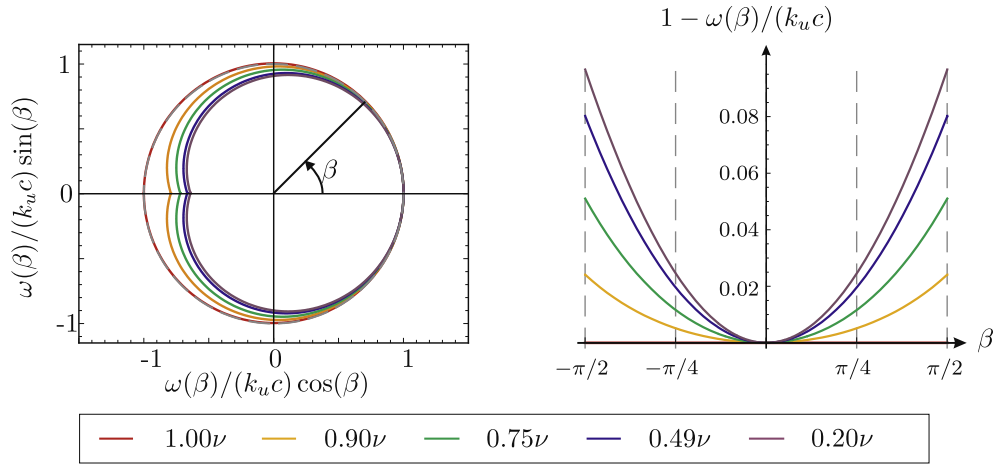

Fig. 14. Polar plot of the normalized angular frequency (left) and the frequency error (right) of the FIT for waves traveling along a coordinate in a one-dimensional domain. The gray dashed unit circle in the left graph indicates the exact solution. The curves correspond to various time steps with respect to the maximally stable CFL number v.

A von Neumann analysis yields the phase and amplification functions

$$\Phi(\omega\Delta t) = \sin(\omega\Delta t), \tag{92}$$

$$A(\omega\Delta t) = \exp(\cos(\omega\Delta t) - 1). \tag{93}$$

Combining these with the spatial phase and amplification properties of the FVMs given in (44)–(49), the dispersion and dissipation relations of the fully discrete longitudinal operator are obtained.

We introduce the CFL number v [8] as

$$v := \frac{c\Delta t}{\Delta u}. \tag{94}$$

Figs. 13–16 show plots of the amplification and normalized angular frequency as well as plots of the errors of those quantities for the fully discretized formulations of all introduced methods. The FIT dispersion graphs in Figs. 13 and 14 correspond to the two- and one-dimensional case. The FVM dispersion and dissipation graphs correspond to the one-dimensional case. For the amplification factor graphs the unit circle corresponds to a neutrally stable, and thus energy conserving, scheme. This is the case for the fully discretized formulation of the FIT for any stable choice of the time step. On the contrary, all FVM formulations exhibit a dissipative character. While Godunov's method shows large amplitude errors, they are small for the Lax-Wendroff and Fromm methods.

For the graphs of the normalized angular frequency, time step dependent deviations from the unit circle imply a dispersive behavior. This is the case for all methods presented. However, dissipation and dispersion errors of the one-dimensional formulations vanish for $v = 1$. Therefore, Δt^{1D}_{max} is often referred to as the magic time step Δt^{*}.

For a stable explicit time stepping, the well-known CFL condition has to be fulfilled. It establishes the time step limits

$$\Delta t^{1D}_{max} = \frac{\Delta u}{c}, \tag{95}$$

$$\Delta t^{2D}_{max} = \frac{\Delta u}{\sqrt{2}c}, \tag{96}$$

for the involved one- and two-dimensional subproblems, respectively. In Fig. 17 exemplary eigenvalue distributions of $\mathbf{T}^G$ and $\mathbf{T}^S$ for Δt^{1D}_{max} are shown. It is not possible to apply the Godunov splitting with this step since it exceeds the time step limit of the two-dimensional FIT subproblem (96). For the Strang scheme, the transverse update is decomposed into two steps, each of them proceeding $\Delta t^{1D}_{max}/2$ in time. Since it holds true

$$\frac{\Delta t^{1D}_{max}}{2} = \frac{\Delta u}{2c} < \frac{\Delta u}{\sqrt{2}c} = \Delta t^{2D}_{max}, \tag{97}$$

the update is expected to be stable. Fig. 17 confirms this statement. Hence, only the Strang split operator method is applicable (cf. Fig. 17) with the magic time step.

The LT-FIT and the FI–FV scheme yield identical results if the magic time step is applied. However, in non-equidistant or locally refined grids the maximum stable time step Δt^{1D}_{max} and the magic time step Δt^{*} coincide only for the smallest cells. In all other cells dispersion effects occur and deteriorate the solution quality.

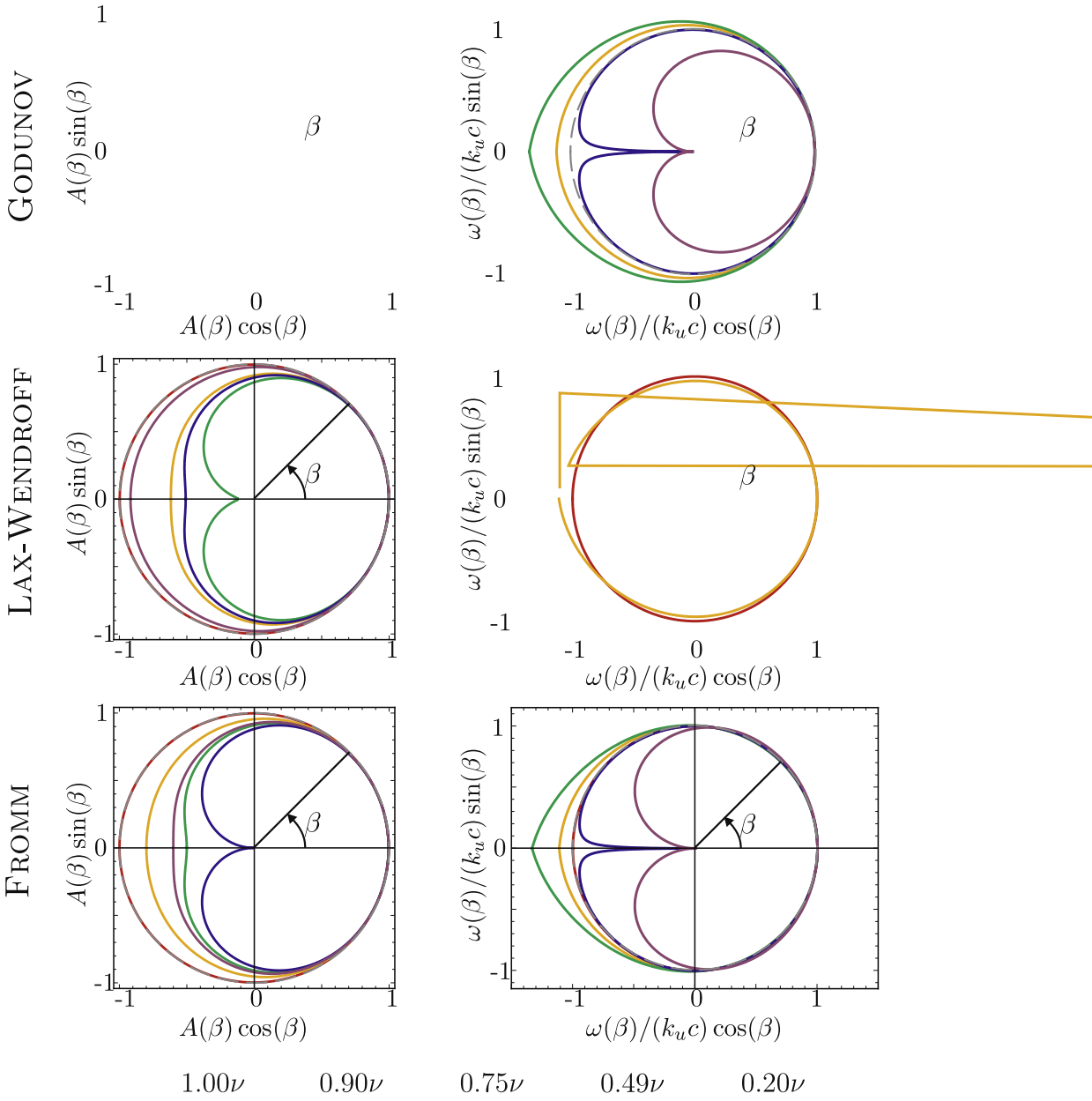

Fig. 15. Polar plots of the amplification (left) and normalized angular frequency (right) of the Godunov, Lax-Wendroff and Fromm schemes. The gray dashed curve indicates the exact solution. Godunov's as well as Fromm's method have no phase error for the CFL numbers 1.0 and 0.5 (in the graphs curves for ν ¼ 0.49 instead of ν ¼ 0.5 are shown). However, for ν ¼ 0.5 damping is at a maximum for these methods.

7. Examples

The FI–FV hybrid scheme is applied to two example problems. As a first illustrative example, the propagation of a cylindrical wave is simulated. The wave is excited by a line current with a Gaussian profile in time, which is truncated at □4σ, where σ is the standard deviation. The excitation is sampled using 16 time steps only. For this poor resolution strong dispersion effects are expected. The field pattern obtained by using the FIT with the maximally stable time step Δt^{2D}_{max} is shown in a cut view in Fig. 18 (top left). It exhibits a fourfold symmetry with respect to the axes. However, the solution is polluted by dispersion errors. For the result shown in Fig. 18 (top right) the LT-FIT scheme was employed using the magic time step Δt^{1D}_{max}. For this particular choice of the time step the FI–FV scheme yields an identical result. This does not hold true anymore in the bottom graphs, where $0.75\Delta t^{1D}_{max}$ was applied. The result shown in the lower left graph was obtained with the LT-FIT

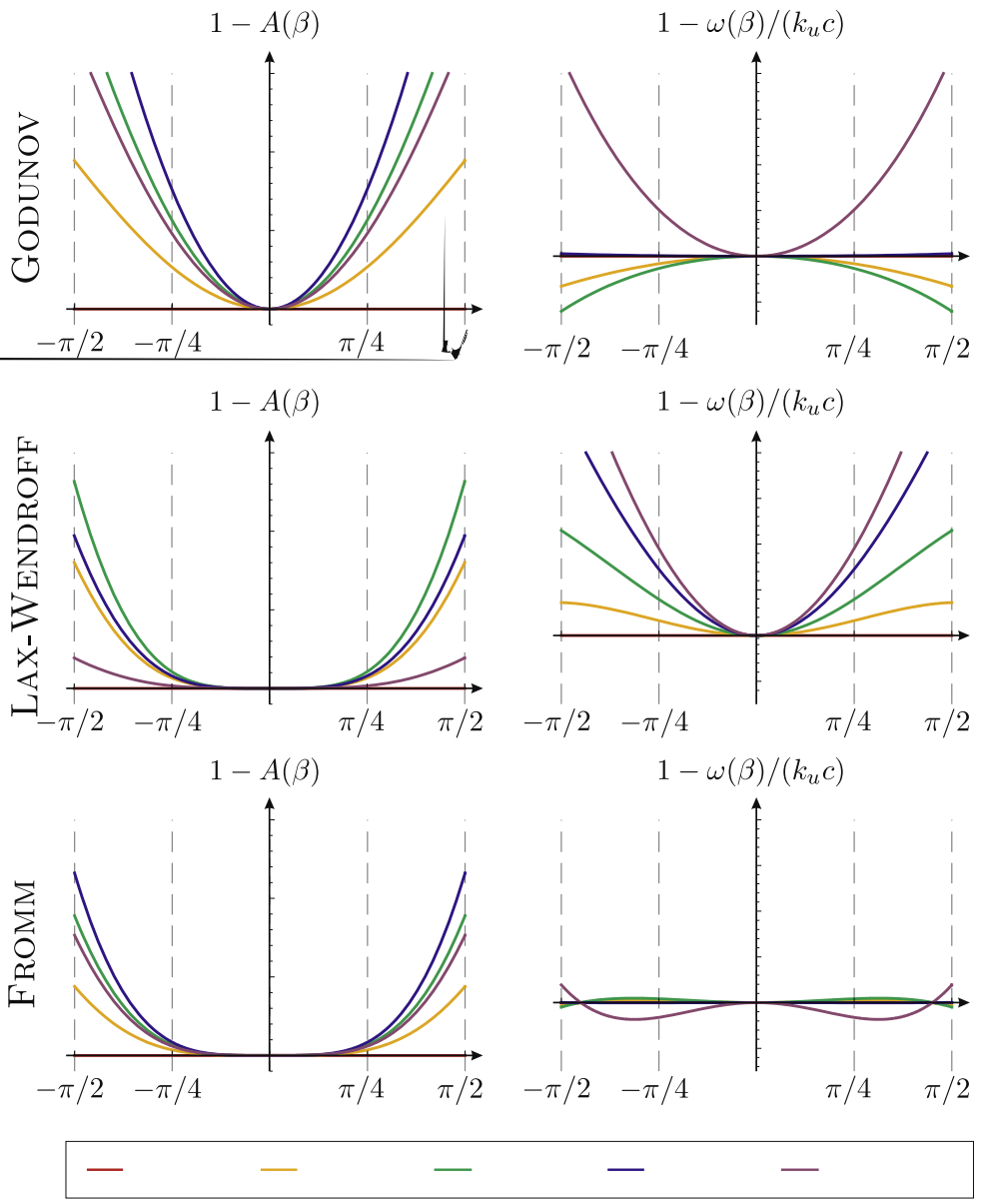

method. The pattern does not show the fourfold symmetry anymore. Nevertheless, dispersion effects emerge along both axes. For the result shown in the lower right graph the FI–FV scheme was applied, also employing a time step of $0.75\Delta t^{1D}_{max}$. Also in this case, dispersion effects occur along both axes, however, they are much less pronounced along the z-axis. In both cases the z-direction was treated as the long direction for the one-dimensional problem. Thus, the FI–FV scheme offers advantages for many real-world problems, where equidistant grids are not applicable. Furthermore, the FI–FV scheme uses about one third less CPU time than the LT-FIT.

Our motivation for developing a scheme with improved dispersion properties along one coordinate was its integration into an existing code, which utilizes time-adaptive mesh refinement. We reported on this development, e.g. in [16,17]. This code has been applied for the simulation of charged particle dynamics in linear particle accelerators. The application of adaptive mesh refinement naturally eliminates the possibility of applying the magic time step in all cells.

In the second example, the FI–FV scheme is applied to the simulation of a bunch of electrons in a rectangular pipe. The electrons travel at the speed of light. Due to the relativistic contraction, the spectrum of the excited electromagnetic fields

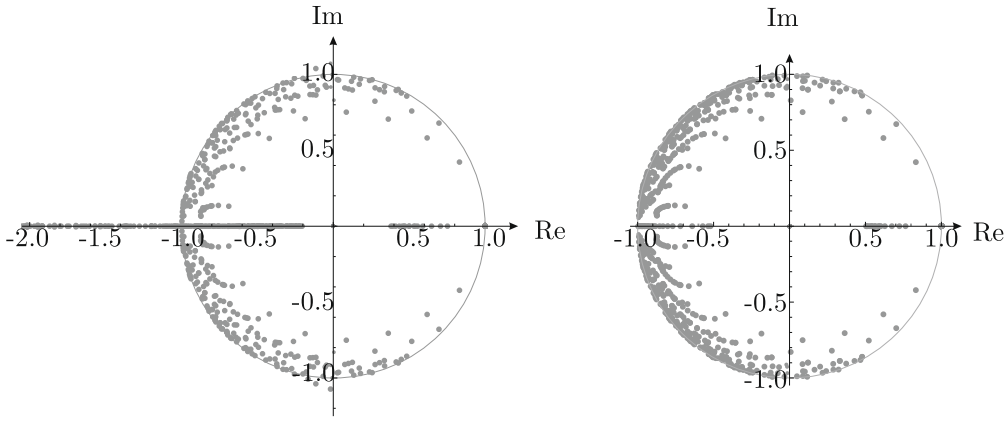

Fig. 17. Exemplary eigenvalue distribution of the FI–FV iteration matrix in the complex plane. In the left hand side graph the Godunov splitting scheme was applied, while in the right hand side graph the Strang scheme was used.

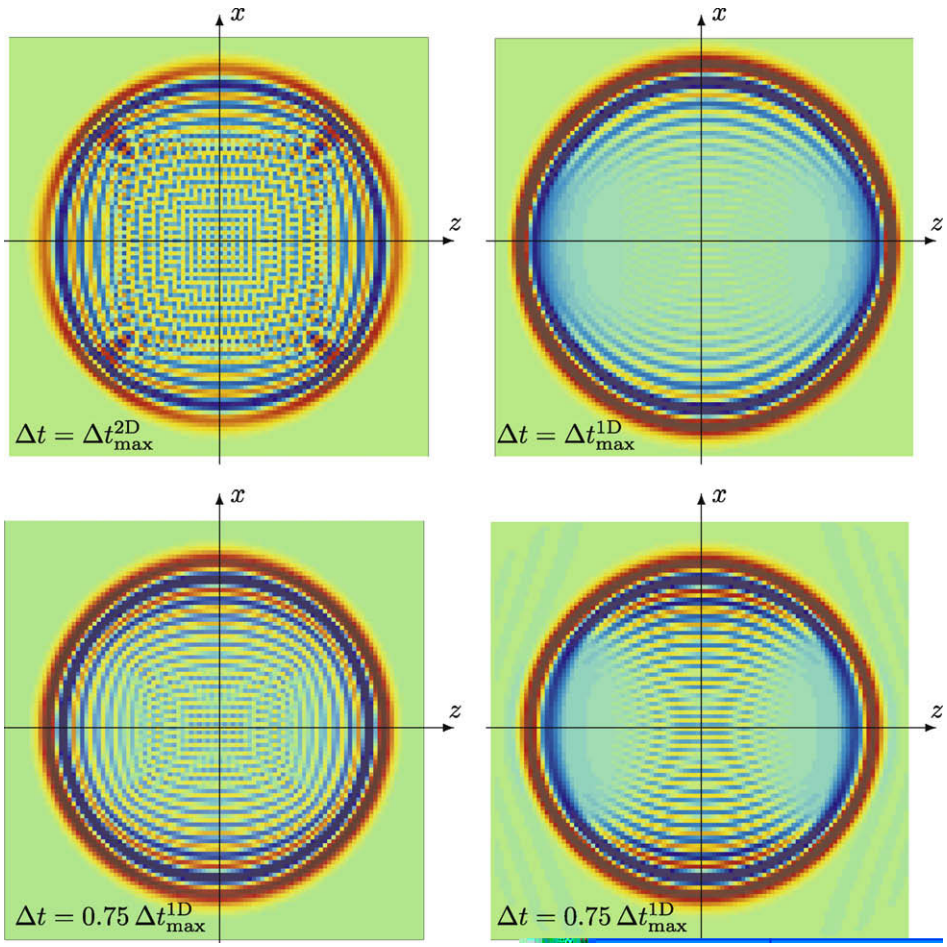

Fig. 18. Cylindrical wave simulated with the FIT, LT-FIT, and FI–FV scheme. The cylindrical wave is excited by a *y*-directed line current located at *x* ¼ 0 and *z* ¼ 0 with a Gaussian time profile. The plot shows the E_y component in a cut view. A very low temporal resolution of the exciting current was chosen. Hence, strong dispersion effects emerge. The upper left result was obtained using the FIT and the upper right result with the LT-FIT. In both cases the respective maximum time step was applied. For the magic time step the LT-FIT and the FI–FV scheme yield identical results. Dispersion effects are limited to the propagation along the *x*-axis, resulting in a clearly non-symmetrical pattern. The results in the lower graphs were obtained with the LT-FIT (bottom left) and FI–FV scheme (bottom right) using a reduced time step (Δt ¼ $0.75\Delta t^{1D}_{max}$). The application of the LT splitting procedure with the FIT offers no benefit if a time step different from the magic one is chosen ð$v < 1$Þ. In the case of the FI–FV scheme, dispersion effects also occur along both axes, however, they are much less pronounced along the *z*-axis.

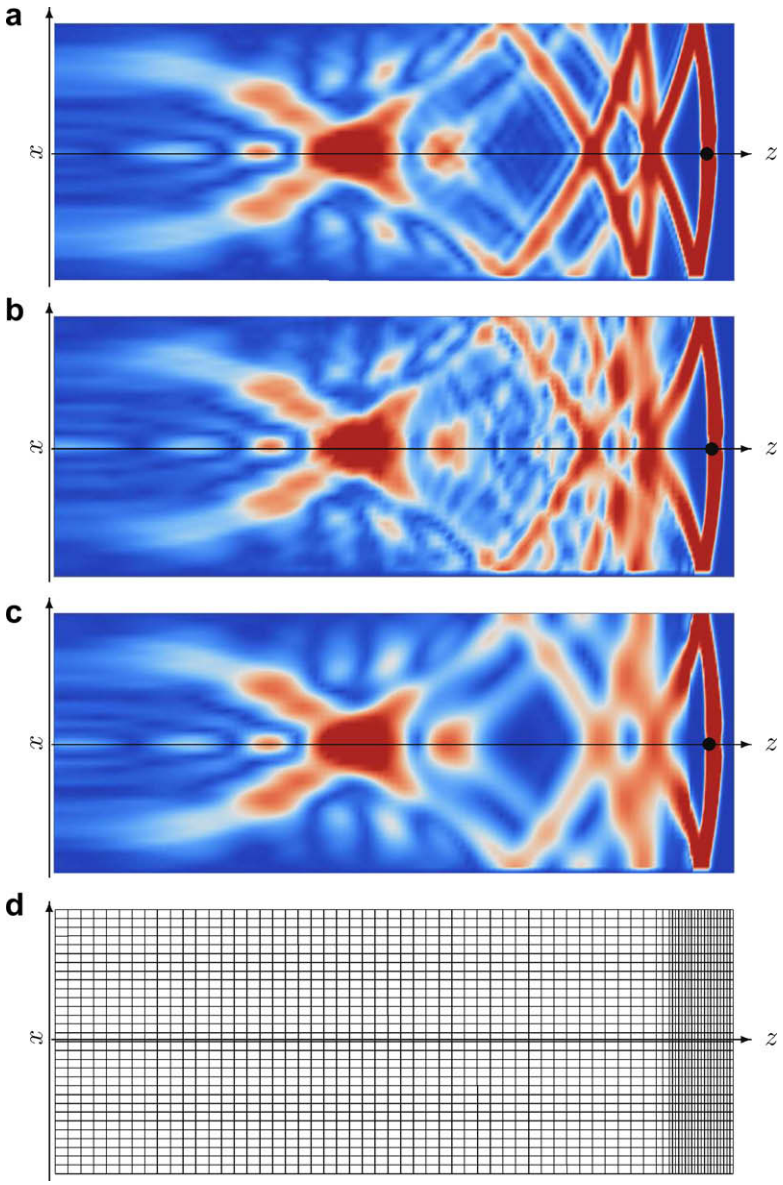

Fig. 19. In (a) to (c) cut views of the total electric field in a rectangular pipe excited by a bunch of electrons (indicated as a black dot) are shown. The electrons travel at the speed of light in z-direction. The result shown in (a) was obtained using the LT-FIT method on a fixed grid and is considered the reference. For (b) and (c) the LT-FIT and FI–FV hybrid scheme were applied on adaptively refined grids. In (d) the adaptively refined grid for the respective instant in time is shown. For this illustration, every second grid line in both directions was omitted. A comparison of (b) and (c) reveals the improved dispersion behavior of the FI–FV scheme with respect to the LT-FIT. The small dispersion errors visible in (a) stem from the dispersion afflicted two-dimensional FIT problem. In (c) also the dissipating character of the FI–FV scheme in the non-refined area is visible.

contains very high frequencies. In Fig. 19 the electric field solutions obtained with LT-FIT on a fixed grid (a), LT-FIT on a time-adaptive grid (b) and the FI–FV scheme on a time-adaptive grid (c) are shown in a cut view. In addition, (d) shows one layer of the adapted grid as employed utilized in (b) and (c) at the respective instant in time. In this illustration every second grid line had to be omitted in order to obtain a visible separation of the lines. The grid was adapted along the z-axis only. The fixed grid used in (a) consists of 45 □ 45 □ 450 ¼ 911250 nodes. For the time-adaptive grids used in (b) and (c) the ratio of the grid step size in z-direction within the maximally refined region and the non-refined grid is 1/4. The grid resolution in the bunch region is identical for all cases (a)-(c) and corresponds to approximately 10 cells along the length of particle bunch.

The improved overall dispersion properties of the FI–FV scheme with respect to the LT-FIT are reflected in the results shown in Fig. 19(b) and (c). While the LT-FIT solution is polluted with dispersion errors, non-physical high-frequency oscillations are barely visible in the FI–FV solution. The graphs in Fig. 20 confirm this statement. There, the total electric field

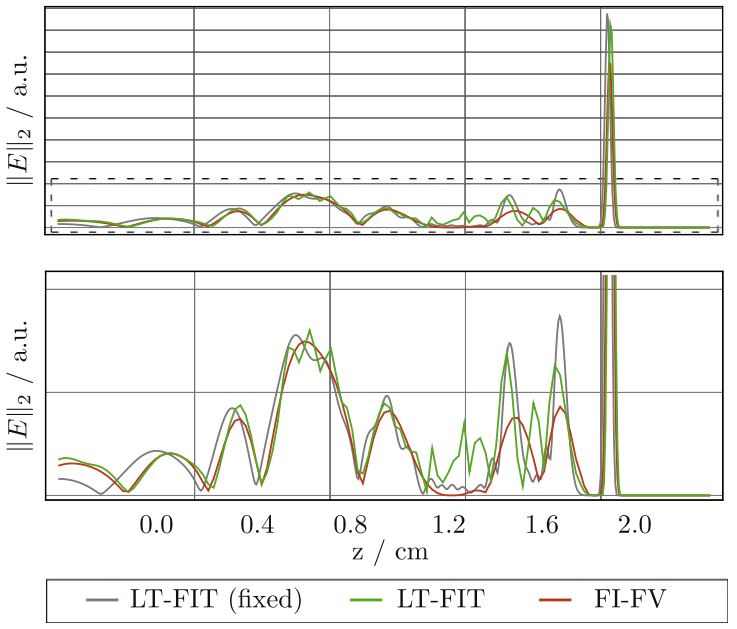

Fig. 20. Plots of the absolute of the electric field along the z-axis of Fig. 19(a)–(c). The bottom graph shows an enlargement of the boxed area in the top graph. The FI–FV result exhibits barely any non-physical oscillatory behavior, which emerges for the other methods due to dispersion errors.

along the z-axis is plotted. The bottom graph shows an enlarged view of the framed area of the top graph. High-frequency oscillations are absent in the FI–FV result.

For simulations involving grid adaptation, the dispersive and dissipative behavior of the discrete solution changes according to the local resolution. The value of β depends locally on the grid step size and corresponds to a certain dispersion and dissipation error according to Figs. 13–16. In order to perform an adaptation of the grid, grid voltages have to split and merged. Due to their definition as integral state variables, this can be done without any error. The grid adaptation does, therefore not additionally affect the propagation behavior.

8. Conclusions

We introduced a hybrid Finite Integration–Finite Volume (FI–FV) Scheme with improved dispersion properties along one coordinate. It is well-suited to the simulation of problems exhibiting a preferred direction, e.g. problems comprising large aspect ratios along the different coordinate axes. The scheme is based on a splitting of the discrete curl operator into a two-dimensional and a one-dimensional operator. The FIT is applied to the former, the FVM to the latter. This yields a hybrid scheme combining the computational efficiency of the FIT with the superior dispersion properties of the FVM. We presented a short review of the FIT and the FVM and summarized their semi-discrete dispersion and dissipation properties. For the FVM, the central, Godunov, Lax-Wendroff, and Fromm flux were considered. We established asymptotic orders of the dispersion and dissipation errors of all considered methods. Subsequently, suitable time integration methods for the semi-discrete equations were presented. We highlighted the relation of the distribution of eigenvalues of the system matrix and the iteration matrix. In this context, we showed that the combination of the upwind flux formulation of the FVM and the leap-frog scheme is always unstable regardless of the chosen time step. Additionally, we showed that the Godunov splitting cannot be applied with the magic time step due to a violation of the stability condition. We, thus, applied the Strang split method. We elaborated on the coupling of the FIT and FVM degrees of freedom and presented a matrix representation of the three-dimensional scheme. The novel scheme was applied to two examples, which confirmed its superior dispersion properties along the preferred direction.

References

[1] T. Weiland, On the unique numerical solution of Maxwellian eigenvalue problems in three dimensions, Part. Accel. 17 (1985) 227–242.
[2] R. Schuhmann, T. Weiland, Conservation of discrete energy and related laws in the finite integration technique, Prog. Electromagn. Res. 32 (2001) 301–316.
[3] P. Colella, E.G. Puckett, Modern Numerical Methods for Fluid Flow, UC Berkeley and UC Davis, 1998.
[4] T. Weiland, Time domain electromagnetic field computation with finite difference methods, Int. J. Numer. Model El 9 (1996) 295–319.
[5] T. Weiland, On the numerical solution of Maxwell's equations and applications in the field of accelerator physics, Part. Accel. 15 (1984) 245–292.
[6] H. Yoshida, Recent progress in the theory and application of symplectic integrators, Celest. Mech. Dyn. Astr. 56 (1993) 27–43.
[7] R.J. LeVeque, Numerical Methods for Conservation Laws, second ed., Birkhäuser, Basel, 1990.

[8] C.B. Laney, Computational Gasdynamics, first ed., Cambridge University Press, Cambridge, 1998.
[9] P. Thoma, Zur numerischen Lösung der Maxwellschen Gleichungen im Zeitbereich, Ph.D. Thesis, TU Darmstadt, 1997.
[10] G. Cohen, Higher-Order Numerical Methods for Transient Wave Equations, first ed., Springer, Berlin, Heidelberg, 2002.
[11] E. Hairer, G. Wanner, Solving Ordinary Differential Equations 1, second ed., Springer, Berlin, 1993.
[12] T. Lau, E. Gjonaj, T. Weiland, Time integration methods for particle beam simulations with the finite integration theory, FREQUENZ 59 (2005) 210–219.
[13] S. Godunov, A finite difference method for the numerical computation and discontinuous solutions of the equations of fluid dynamics, Mat. Sb. 47 (1959) 271–306.
[14] G. Strang, On the construction and comparison of difference schemes, SIAM J. Numer. Anal. 5 (1968) 506–517.
[15] E. Gjonaj, T. Lau, S. Schnepp, F. Wolfheimer, T. Weiland, Accurate modelling of charged particle beams in linear accelerators, New J. Phys. 8 (2006) 1–21.
[16] S. Schnepp, E. Gjonaj, T. Weiland, A time-adaptive mesh approach for the self-consistent simulation of particle beams, in: Proc. 9th Int. Comp. Accel. Phys. Conf., 2006, pp. 132–135.
[17] S. Schnepp, E. Gjonaj, T. Weiland, Analysis of a particle-in-cell code based on a time-adaptive mesh, in: Proc. Part. Accel. Conf., 2007, pp. 3271–3273.